Clustering of Marine Oil-Spill Extent Using Sentinel-1 Dual-Polarimetric Scattering Spectrum

Avrodeep Paul, *Member, IEEE*, Subhadip Dey, *Member, IEEE*, Armando Marino, *Member, IEEE*, Gourav Dhar Bhowmick, and Avik Bhattacharya, *Senior Member, IEEE*

***Abstract*—Oil spills pose a significant threat to the maritime ecosystem. Identifying an oil spill is vital to assess its spread and drift to nearby coastal areas. Synthetic aperture radar (SAR) sensors are viable for mapping and monitoring marine oil spills. This study proposes a new technique that utilizes the dual-polarimetric Sentinel-1 SAR data. The method is based on projecting the 2×2 covariance matrix onto distinct random realizations of the normalized scattering configuration. We then obtain the dual-polarimetric spectrum of the scattering-type parameter, θ_{DP}. The θ_{DP} spectrum is then used in the unsupervised K-means clustering technique to segment oil spills from the rest. The cluster findings are then compared to the accuracies obtained using the standard scattering-type parameters from the eigen-decomposition approach (VV, VH) intensities and Otsu thresholding of $[H + \alpha + A]$ parameter. We demonstrate the proposed approach by clustering marine oil-spill extent over parts of India, Kuwait, the UAE, and the Mediterranean Sea obtained by Sentinel-1 SAR images. We observed that the clustering accuracy of the proposed technique outperforms the ones obtained from the channel (i.e., VV and VH) intensities, Otsu thresholding of $[H + \alpha + A]$ parameter, and the eigen-decomposition-based method. The proposed approach improves the overall accuracy by $\approx 8\%$ and $\approx 20\%$, respectively, over different study areas.**

***Index Terms*—Dual-polarized synthetic aperture radar (SAR), K-means clustering, oil spill (OS), Sentinel-1, unsupervised classification.**

I. Introduction

OIL pollution of open-ocean and coastal waters are major threats to the marine environment [1], [2]. The occurrence of these oil spills (OSs) is unpredictable, and they might be accidental or intentional. Tanker accidents are the most common cause of large OSs, accounting for 8% of oil pollution according to [3]. However, unlawful discharges of greasy ballast water, tanker washing residue, fuel oil sludge, engine waste, and foul bilge water are the principal source of human-caused oil pollution.

OS monitoring is mainly performed using satellite-based optical datasets [4]. However, one of the most challenging aspects of using optical data is cloud cover. Thick cloud cover is frequently observed over high ocean areas and coastal seas. As a result, optical sensors cannot offer information in these circumstances. Alternatively, synthetic aperture radar (SAR) images, on the other hand, are largely independent of cloud cover and illumination sources. Traditionally, OSs were monitored with single polarized SAR data [5], [6].

In recent years, several quad-polarized and dual copolarized datasets have improved OS detection accuracy [7], [8]. In the quad-polarized case, two orthogonal polarizations are alternatively transmitted and received, i.e., HH, HV, VV, and VH, where H denotes horizontal, and V denotes vertical polarizations. Nunziata et al. [9] proposed a quad polarimetric model using the Muller matrix to characterize the scattering from oil and biogenic slicks over the ocean surface. The elements of the Muller matrix from the oil-slick area were found to be different from the slick-free site. Later, Migliaccio et al. [10] developed a model to detect OSs using the copolarized phase difference for low to medium wind speed conditions. It was found that the phase difference was able to separate the OS from other biogenic look-alikes.

In general, on sea surfaces, Bragg-type scattering dominates SAR backscatter [11]. This Bragg-type scattering occurs mostly for incidence angles between 20° and 70°. However, OSs form a thin layer on top of the ocean surface, which dampens waves, causing a dark appearance in the radar images. Guo and Zhang [12] extracted nine shape features and different eigenvalues to detect OSs using the ERS-1, ERS-2, and ENVISAT data. Comparable eigenvalues were extracted using differential evolution feature selection, and incorrect eigenvalues were deleted, resulting in more accurate identification. Similarly, numerous automated and semiautomated strategies for OS detection have been presented in the literature [13], [14], [15], [16].

Although quad polarimetric data gives superior discrimination capabilities, its main shortcoming is its scarcity and narrow swath width. The authors in [17] and [18] studied the characteristics of an OS event in the Al Khafji region using Sentinel-1 SAR images. It was concluded that the VV channel is more sensitive than the VH channel for detecting OSs. Similarly, Chaturvedi et al. [19] indicated that the VV polarization channel is better than VH for distinguishing OSs.

Manuscript received 5 July 2023; revised 4 September 2023; accepted 8 September 2023. Date of publication 13 September 2023; date of current version 3 October 2023. *(Corresponding author: Subhadip Dey.)*

Avrodeep Paul, Subhadip Dey, and Gourav Dhar Bhowmick are with the Agricultural and Food Engineering Department, Indian Institute of Technology Kharagpur, Kharagpur 721302, India (e-mail: avrodeeppaul1998@gmail.com; sdey2307@gmail.com; gourav.db@gmail.com).

Avik Bhattacharya is with the Microwave Remote Sensing Lab, Center of Studies in Resources Engineering, Indian Institute of Technology Bombay, Mumbai 400076, India (e-mail: avikb@csre.iitb.ac.in).

Armando Marino is with the Earth Observation, Biological and Environmental Sciences, University of Stirling, FK9 4LA Stirling, U.K. (e-mail: armando.marino@stir.ac.uk).

Digital Object Identifier 10.1109/JSTARS.2023.3314899

The contrast between VV and VH channels can be used to differentiate OSs from the clean ocean surface. Later, amplitudes and intensities of VV and VH channels were used along with the CFAR algorithm on the raw Sentinel-1 data [20]. Subsequently, the Euclidean and J-M distances were used to filter the dominant features from the Sentinel-1 SAR data [21]. The same study found that the polarimetric span, polarimetric entropy [22], and the second-order moment performed well for the classification of OS using the modified K-means clustering algorithm.

Subsequently, El-Magd et al. [23] studied more than 20 OS events over the Suez Canal using five years of data starting from 2014 to 2019. In their study, a dark spot-based analysis was adopted for detection purposes. Mdakane and Kleynhans [24] extracted texture, physical, and spatial features along with the multiple feature selection method and gradient boosting tree classifier to select, classify, and determine significant features for determining the OS areas. Rajendran et al. [25] compared both Sentinel-1 and Sentinel-2 data for the classification of spill area and observed that the classification accuracy differs by only 7% from Sentinel-1 to Sentinel-2 images. A contamination probability model of the OS area over the Caspian region showed that the contamination probability is more than 50% in the shoreline range of 464–508 km [26]. Besides, Li et al. [27] proposed a multiscale conditional adversarial network to identify the large area of OS using ERS-1, ERS-2, and ENVISAT-1 satellite data. Similarly, an adversarial learning approach is implemented to forecast the wind field correction and OS drift detection [28]. Later several machine learning algorithms were utilized for detecting the OS using Sentinel-1 data [29], [30], [31], [32].

Therefore, it can be seen from the literature that all of the previous studies used only the received linear polarimetric SAR information to identify the spilled areas. However, the information contained only in a linear basis might be similar to both spilled and ocean surface areas. As a result, the overall accuracy drops, particularly over the marine spilled area. In this context, a polarimetric spectrum might overcome this situation as the projections onto several scattering bases exhibit diverse scattering characteristics of a target, as shown by Dey et al. [33]. In this study, we have extended the concept of the polarimetric spectrum first proposed in [33] to the dual-polarimetric (DP) case (VV-VH). Notably, the polarimetric spectrum helps to distinguish the targets with a single statistical parameter instead of several statistical parameters, such as the scattering entropy (H) and the scattering-type parameter $\overline{\alpha}$ derived from the SAR data. Dey et al. [33] found an enhancement in the overall classification accuracy over different targets by using the polarimetric spectrum compared to the eigen-based techniques. Furthermore, unlike other learning strategies, our suggested technique is purely based on the physical features of the target and hence nearly independent of sample data distributions. We have used dual-pol Sentinel-1 data over the OS area of Al Khafji in Kuwait, the Al-Fujairah coast in United Arab Emirates (UAE), the Ennore OS in India, and the Northern entrance of the Suez Canal in the Mediterranean Sea. The wind speed information of the data sources used in this study is acquired from https://earth.nullschool.net/ [34].

II. Methodology

A. Scattering Type Parameter

In DP SAR, the complex scattering vector encompasses polarimetric information about the backscattering from targets in each pixel using a linear horizontal or vertical basis. It is expressed in the backscatter alignment convention in the linear horizontal (H) and linear vertical (V) polarization basis as

$$\vec{\boldsymbol{k}}_{\boldsymbol{H}} = \begin{bmatrix} S_{\mathrm{HH}} & S_{\mathrm{HV}} \end{bmatrix} \tag{1}$$

$$\vec{\boldsymbol{k}}_{\boldsymbol{V}} = \begin{bmatrix} S_{\mathrm{VH}} & S_{\mathrm{VV}} \end{bmatrix} \tag{2}$$

where $\vec{\boldsymbol{k}}_{\boldsymbol{H}}$ and $\vec{\boldsymbol{k}}_{\boldsymbol{V}}$ are the scattering vectors in horizontal or vertical-transmit bases. The 2×2 covariance matrix $\mathbf{C}_2$, which is an ensemble average of $\vec{\boldsymbol{k}}_{\boldsymbol{H}}$ or $\vec{\boldsymbol{k}}_{\boldsymbol{V}}$, with its conjugate transpose $\vec{\boldsymbol{k}}_{\boldsymbol{H}}{}^{*T}$ or $\vec{\boldsymbol{k}}_{\boldsymbol{V}}{}^{*T}$ provides the second-order information. Thus, $\mathbf{C}_2^{\mathrm{H}} = \langle \vec{\boldsymbol{k}}_{\boldsymbol{H}}\, \vec{\boldsymbol{k}}_{\boldsymbol{H}}{}^{*T} \rangle$ or $\mathbf{C}_2^{\mathrm{V}} = \langle \vec{\boldsymbol{k}}_{\boldsymbol{V}}\, \vec{\boldsymbol{k}}_{\boldsymbol{V}}{}^{*T} \rangle$ and these matrices are generally rank-2.

Let us now define an arbitrary 2×1 complex vector $\vec{\boldsymbol{\omega}}$ as

$$\vec{\boldsymbol{\omega}} = \begin{bmatrix} Ae^{i\phi_1} \\ Be^{i\phi_2} \end{bmatrix} \tag{3}$$

where A and B are the magnitudes of each component and ϕ_1 and ϕ_2 are corresponding phases. Following this, the normalized complex vector $\vec{\boldsymbol{\omega}}_n = \vec{\boldsymbol{\omega}}/|\vec{\boldsymbol{\omega}}|$ is projected over the covariance matrix $\mathbf{C}_2^{\mathrm{H}}$ or, $\mathbf{C}_2^{\mathrm{V}}$ as

$$\vec{\boldsymbol{\omega}}_s = \mathbf{C}_2^{\mathrm{H}} \vec{\boldsymbol{\omega}}_n \tag{4}$$

or,

$$\vec{\boldsymbol{\omega}}_s = \mathbf{C}_2^{\mathrm{V}} \vec{\boldsymbol{\omega}}_n. \tag{5}$$

In this way, $\mathbf{C}_2$ can be projected onto any arbitrary scattering basis by varying $\vec{\boldsymbol{\omega}}_n$. Immediately, it can be noted that, $\langle \vec{\boldsymbol{\omega}}_n^* \vec{\boldsymbol{\omega}}_s \rangle \geq 0$ as $\mathbf{C}_2$ is positive semidefinite matrix. Besides, if $\vec{\boldsymbol{\omega}}_n^{*T} \mathbf{C}_2 \vec{\boldsymbol{\omega}}_n = 1$, then $\vec{\boldsymbol{\omega}}_s = \vec{\boldsymbol{\omega}}_n$.

This projected vector $\vec{\boldsymbol{\omega}}_s$ is now used to compute a higher order rank-1 covariance matrix, $\mathbf{C}_2$. This $\mathbf{C}_2$ matrix is calculated as the ensemble average of the outer product of $\vec{\boldsymbol{\omega}}_s$ and its conjugate transpose $\vec{\boldsymbol{\omega}}_s^{*T}$

$$\mathbf{C}_2^s = \left\langle \vec{\boldsymbol{\omega}}_s \vec{\boldsymbol{\omega}}_s^{*T} \right\rangle. \tag{6}$$

In this case, $\mathbf{C}_2^s$ is a rank-1, Hermitian, positive semidefinite matrix. Because $\mathbf{C}_2^s$ contains higher order covariance information, we use the following theorem to transform it into a second-order covariance structure.

Theorem 1: Let $\mathbf{A}$ be a positive semidefinite matrix (real or complex). Then, there is precisely one positive semidefinite (and hence symmetric) matrix $\mathbf{B}$ such that $\mathbf{A} = \mathbf{B}^*\mathbf{B}$.

With Theorem 1 $\mathbf{C}_2^s$ can be written as, $\mathbf{C}_2^s = \mathbf{C}_2^{p*} \mathbf{C}_2^p$. To obtain the matrix square root, we used the Schur factorization method. Thus, $\mathbf{C}_2^p$ is unique and known as the principal square root matrix. Besides, as $\mathbf{C}_2$ is the outer product of the Lexicographic basis matrix, $\mathbf{C}_2^p$ can be inherently related to a canonical target representation in the same basis without any scale dependency. Hence, $\mathbf{C}_2^p$ will also be able to characterize diverse properties of the targets.

Following this, the scattering-type parameter, θ^p_{DP} is derived from the elements of $\mathbf{C}^p_2$ as proposed by Dey et al. [35] as

$$\theta^p_{\mathrm{DP}} = \tan^{-1} \frac{m_{\mathrm{DP}}\,\mathrm{Span}\,(C_{11} - C_{22})}{C_{11}C_{22} + m^2_{\mathrm{DP}}\,\mathrm{Span}^2} \tag{7}$$

where m_{DP} is the 2-D degree of polarization given by Barakat [36] and C_{11} and C_{22} are the diagonal elements of $\mathbf{C}^p_2$ with $\mathrm{Span} = C_{11} + C_{22}$.

The 2-D Barakat degree of polarization, m_{DP}, like the basis-invariant conventional degree of polarisation, characterizes different polarisation states of the scattering EM wave from the targets. In this aspect, a fully polarised wave has $m_{\mathrm{DP}} = 1$, whereas a fully depolarized wave has $m_{\mathrm{DP}} = 0$. For any other partial polarizations, $0 < m_{\mathrm{DP}} < 1$. Nonetheless, for rank-1 $\mathbf{C}^p_2$, $m_{\mathrm{DP}} = 1$.

The range of θ^p_{DP} varies from $-45°$ to $45°$. The spectrum of θ^p_{DP} is generated by arbitrarily varying $\vec{\omega}_n$. Therefore, these realizations of $\vec{\omega}_n$ are representative scattering mechanisms.

B. K-Means Clustering

The K-means clustering technique is an unsupervised learning algorithm to separate data points into different groups based on their similarity measures [37], [38]. Here, "K" denotes the number of clusters that the user predefines. Initially, K cluster centroids are selected randomly from the data points. For each data point, the distances from the centroids are calculated. Following this, the data point is assigned to the centroid with the lowest distance. In this way, K numbers of clusters are formed. Now, the centroids of each K cluster are recalculated until the centroids converge. The performance generally depends on the initial centroid selection.

C. T-Distributed Stochastic Neighborhood Embedding (t-SNE)

In order to effectively visualize data points, t-SNE employs a nonlinear dimensionality reduction technique by embedding high-dimensional space into smaller dimensions. [39]. In t-SNE, the cost function is used to evaluate the degree of divergence in the feature distribution. t-SNE aims to select highly comparable and lowly different points inside the high dimensional space. The point distributions in high and low dimensions are as similar as possible, minimizing the Kullback–Leibler divergence.

III. Study Area and Dataset

A. Indian Test Site

The Indian test site is located on the eastern coast of South India, as shown in Fig. 1. This study area is near the Ennore Port in the city of Chennai (13°8'19.98"N, 80°28'17.28" E). Ennore Creek is a stretch of swampy backwater that separates the town of Ennore from the Kamarajar Port, located on the southern bank of the Kosasthalaiyar River and flows into the Bay of Bengal. On January 27, 2017, an unfortunate collision happened between two ships near the Coromandel Coast of Chennai [40], [41].

Sentinel-1 acquired an image of this area on January 29, 2017. During this time, the average wind speed recorded was 5.2 ms^{-1}. We denote the OS extent in red and the ocean in blue. The

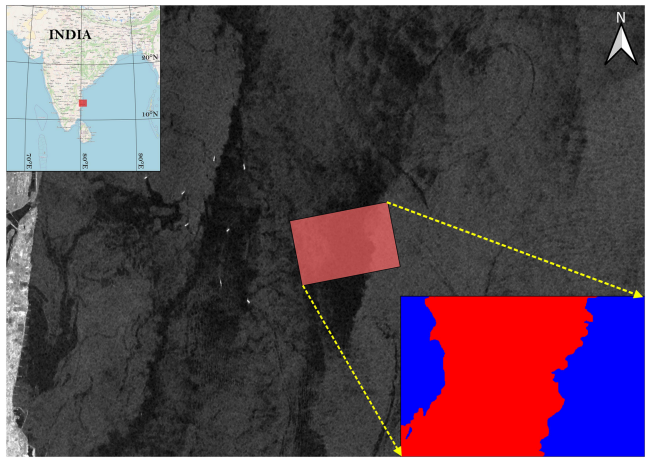

Fig. 1. Sample OS area over the Indian coast near Ennore Port in Chennai. The acquisition date of the Sentinel-1 data is January 29, 2017. The OS area is denoted in red colour, while the waterbody is marked in the blue area.

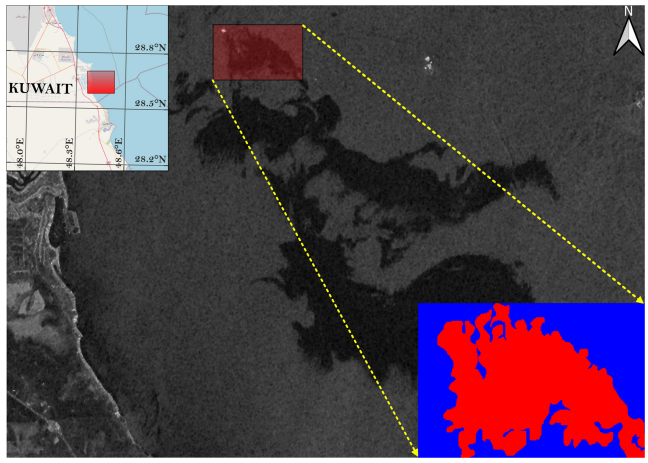

Fig. 2. In Kuwait, the Al Khafji coastline zone along the Persian Gulf is a well-known OS region. A Sentinel-1 image was first collected on August 10, 2017. The region affected by the OS is shown in red, while the adjacent waterbody is shown in blue.

details about the Sentinel-1 image are given in Table I. The range spacing and azimuth spacing of the acquired Sentinel-1 image in Interferometric Wide (IW) Swath mode are 2.32 m and 14 m, respectively, whereas the incidence angle ranges between 30.89° and 36.72°. This single-look complex (SLC) image is multilooked with 6×1 in range and azimuth directions to generate a square pixel and to increase the signal-to-noise ratio. In addition, the image is despeckled with a 7×7 Lee Sigma filter to maintain cell resolution while removing edge sharpness.

B. Kuwait Test Site

The Al Khafji OS located at (28°;76' N, 48°;88' E) in the Persian Gulf is shown in Fig. 2. The slick of oil can be seen in the Sentinel-1 SLC image acquired on August 10, 2017. The average wind speed on this particular date was reported as 3.5 ms^{-1}. Several barrels of oil per day get produced around the area.

TABLE I
DESCRIPTION OF THE SENTINEL-1 DATA OVER THE DIFFERENT STUDY AREAS

Place	Data Name	Satellite data acquisition date	Orbit	Mode	Incidence angle range (deg.)	Resolution (rg × az)
India	S1A_IW_SLC__1SDV_20170129T003131_20170129T003158_015039_01892E_2C18	January 29, 2017	Descending	IW	30.89-36.72	2.32 m × 14 m
Kuwait	S1A_IW_SLC__1SDV_20170810T024712_20170810T024738_017855_01DEF7_445E	August 10, 2017	Descending	IW	30.74-36.74	2.32 m × 13.95 m
UAE	S1A_IW_SLC__1SDV_20170308T142433_20170308T142459_015602_019A78_BCCF	February 8, 2017	Ascending	IW	30.75-36.84	2.32 m × 13.96 m
Mediterranean Sea	S1A_IW_SLC__1SDV_20141004T154823_20141004T154851_002682_002FE4_C094	October 4, 2014	Ascending	IW	30.68-36.75	2.32 m × 13.94 m

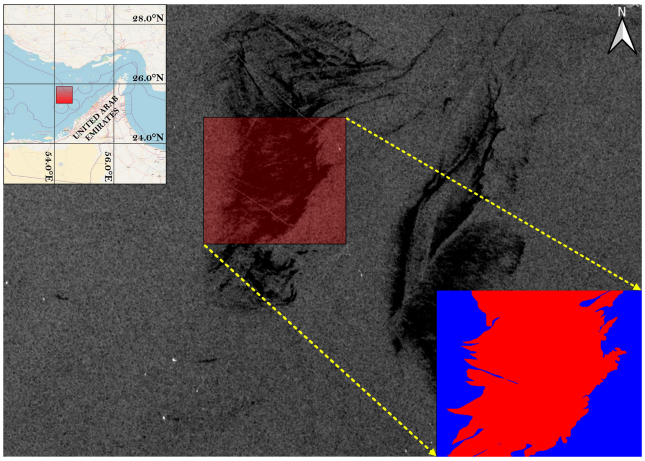

Fig. 3. Arabian Gulf, close to the UAE Al-Fujairah coast. Sentinel-1 acquired the image on March 8, 2017. The region contaminated by the OS is shown in red, while the surrounding waterbody is shown in blue.

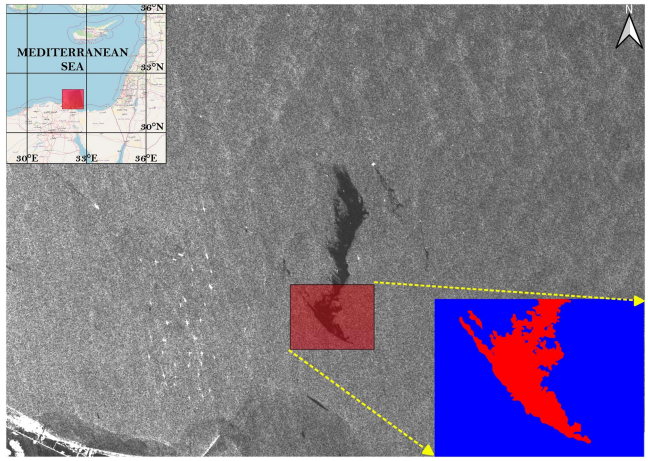

Fig. 4. Mediterranean Sea, close to the Damietta Port Said Coast, Suez Canal. Sentinel-1 acquired the image on October 4, 2014. The region contaminated by the OS is shown in red, while the surrounding waterbody is shown in blue.

During an unfortunate accident, many barrels of crude oil have leaked into the waters of Al-Zour [19], [42], [43], [44].

We have provided the details of the Sentinel-1 image in Table I. The image is acquired in the descending orbit in the IW mode with an incidence angle between 30.74° and 36.74°, and a range spacing to azimuth spacing of 2.32 m and 13.95 m, respectively.

C. UAE Test Site

On March 8, 2017, there was an OS in the Arabian Gulf near the west coast of the UAE (25°46'39.92" N, 54°24'47.24" E). The oil reached the coast of Al-Fujairah [45], [46]. The Sentinel-1 SAR image on 8 March, as seen in Fig. 3, shows the OSs in the Gulf. The average wind speed of this particular study area on the acquired date was measured as 4 ms^{-1}.

Table I provides information about the Sentinel-1 image acquired in the IW swath mode. It has an ascending orbit with an incidence angle ranging between 30.75° and 36.84° and a range spacing to azimuth spacing of 2.32 m and 13.96 m, respectively.

D. Mediterranean Sea Test Site

The study area over the Mediterranean Sea is located between 31°40'14" N, 32°7'13" E. The massive Suez Canal connects the Red Sea and the Mediterranean Sea. Due to its unique geographic location, it is the fastest route for maritime commerce and cargo movement, especially crude oil from the Arab region to Europe and the United States of America [47]. Fig. 4 shows the study area. Here, oil slicks are likely due to shipping loads [48].

The typical wind speed in the research area was measured as 2.3 ms^{-1}. Sentinel-1 SLC image acquired on October 4, 2014 shows the OS. In Table I, we have outlined the specifics of the acquired Sentinel-1 data. The image was captured in the IW swath mode in an ascending orbit with an incidence angle between 30.68° and 36.75° and a range spacing to azimuth spacing of 2.32 m and 13.94 m, respectively.

IV. RESULTS AND DISCUSSION

A. Analysis Over Different Targets

This section analyzes the variation of θ^p_{DP} over the different OSs in the test sites mentioned above. The histograms shown in Fig. 5 are generated using 1000 random realizations of the normalized scattering configuration $\vec{\omega}_n$. Fig. 5(f)–(h) depicts pixels of the OS over the three study areas. Fig. 5(a)–(d) depicts pixels over the waterbody.

It is well known from the literature [49] that one gets Bragg or tilted-Bragg scattering from the sea surface without any oil slick when low-to-moderate wind conditions hold. We obtain a single reflection scattering mechanism from these areas. On the contrary, a weak-dampening OS-covered area or an entire oil-covered sea surface shows low backscattering intensity depicting random scattering.

Often sea surface is considered reflection symmetric. Hence, one expects a very low correlation between the co-pol and cross-pol channels. Moreover, the intensity in the co-pol channel remains much higher than in the cross-pol channel. As a result, we have observed a left tail in the Histogram of θ^p_{DP} from the waterbody pixels. Notably, the median values of all histograms are centered around $40^\circ \pm 2.6^\circ$, depicting nearly coherent scattering characteristics from the waterbody.

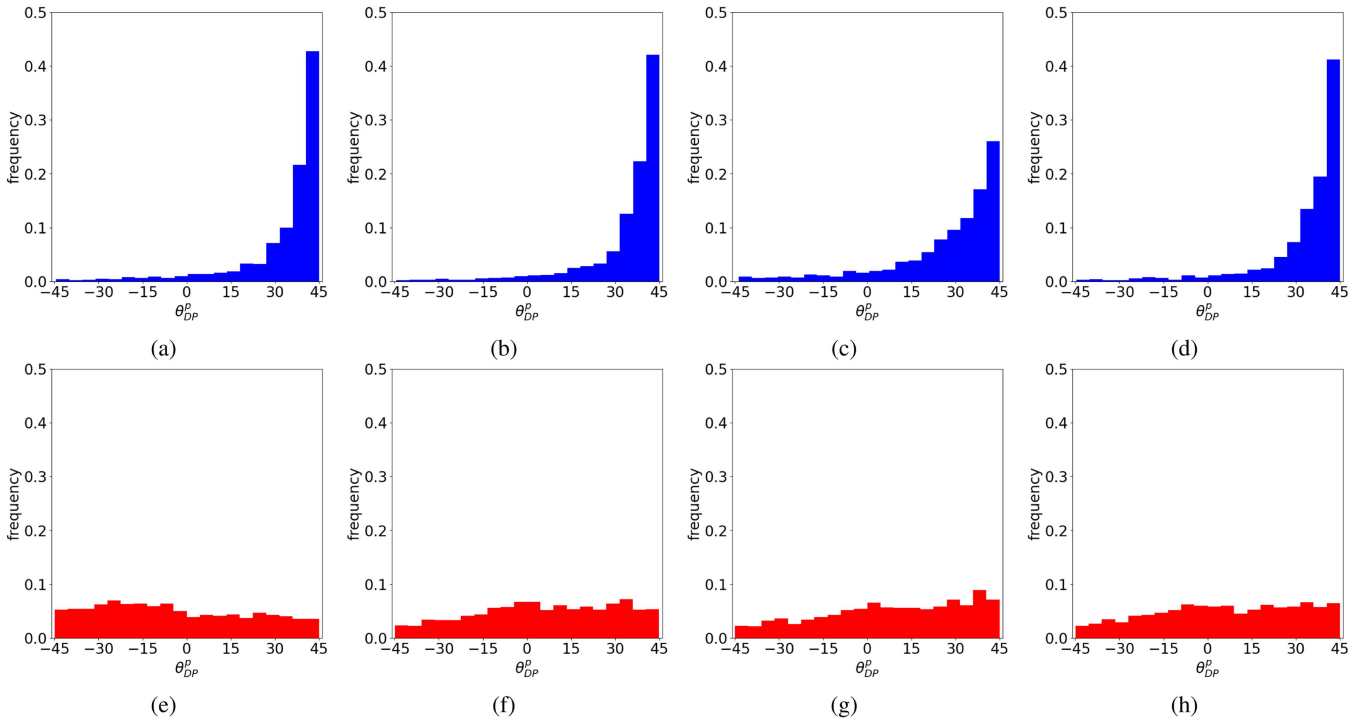

Fig. 5. Histogram of θ^p_{DP} for different targets of four waterbody pixels (a, b, c, d) and another four OS pixels (e, f, g, h) using dual-pol Sentinel-1 C-band data.

Besides, the coefficient of variation of the dual-pol backscatter also remains low. However, the skewness of the Histogram depends on the wind speed over the ocean surfaces during the time of acquisitions for waterbody as -1.95, -1.87, and -2.34, while for OS as 0.20, -1.14, and 0.09. The wind over the ocean surface has possibly generated a certain amount of cross-pol intensity, due to which some values of θ^p_{DP} are lower than 40°.

Over the OS area, we observed an interesting change in the scattering characteristics. In particular, we often describe OS as a reflection symmetric target. However, the backscatter intensity becomes very low due to the moderate to high dampening coefficient in the OS area. As a result, both co-pol and cross-pol intensities get severely affected.

B. Analysis Over Test Sites

In this work, we have used Sentinel-1 scenes over four study areas in India, Kuwait, the UAE, and the Mediterranean Sea. We have generated the ground truth by using the Google Earth images, as shown in Figs. 1–3, respectively, and as proposed by [6], [50]. We employed a K-means unsupervised clustering approach to discriminate marine OS from the water surface (W).

We have compared the results between θ_{DP} values derived from the eigen decomposition, i.e., $(\theta^1_{\mathrm{DP}}, \theta^2_{\mathrm{DP}})$ and the θ^p_{DP} spectrum. Besides, we have shown the results using (VV, VH) intensities. In addition to this, we have compared the results with the existing $[H + \alpha + A]$ parameter along with the Otsu thresholding technique as described by Liu et al. [51]. Here, H denotes entropy, α is the target characterization parameter, and A is anisotropy or the degree of polarization for the dual-pol case.

TABLE II
ACCURACY SCORES OVER DIFFERENT TARGETS USING $(\theta^1_{\mathrm{DP}}, \theta^2_{\mathrm{DP}})$, θ^p_{DP} SPECTRUM, AND (VV, VH) INTENSITIES FOR THE SENTINEL-1 DATA OVER THE INDIAN STUDY AREA

	Overall Accuracy (%)	Omission error (%)		Commission error (%)		Kappa
		Water	OS	Water	OS	
$(\theta^1_{\mathrm{DP}}, \theta^2_{\mathrm{DP}})$	61.67	5.06	64.07	46.59	9.83	0.28
θ^p_{DP} **spectrum**	88.22	12.4	11.29	14.28	9.76	0.76
(VV, VH) intensities	81.67	16.8	15.48	12.41	9.31	0.74
$[H + \alpha$ **+ A] (Otsu)** [51]	84.79	14.41	13.47	19.22	11.23	0.72

In order to obtain $(\theta^1_{\mathrm{DP}}, \theta^2_{\mathrm{DP}})$, we first perform an eigen decomposition of the 2×2 covariance matrix ($\mathbf{C}_2$). Following this, we obtain two rank-1 positive semidefinite Hermitian covariance using the two orthogonal eigenvectors. We then generate the two quantities: $(\theta^1_{\mathrm{DP}}$ and $\theta^2_{\mathrm{DP}})$ from the rank-1 covariance matrices given in (7).

The results using $(\theta^1_{\mathrm{DP}}, \theta^2_{\mathrm{DP}})$ and θ^p_{DP} spectrum over the Indian test site is shown in Table II. The overall accuracy using $(\theta^1_{\mathrm{DP}}, \theta^2_{\mathrm{DP}})$ is 61.67%, while using θ^p_{DP} spectrum is 88.22%. For (VV, VH) intensities, the overall accuracy is 7% lower than θ^p_{DP} spectrum, while for $[H + \alpha + \mathrm{A}]$ based clustering the overall accuracy is $\approx 4\%$ lower than θ^p_{DP} spectrum. We have also observed a significant increase ($\approx 30\%$) in the accuracy over the waterbody using $(\theta^1_{\mathrm{DP}}, \theta^2_{\mathrm{DP}})$ as compared to θ^p_{DP} spectrum. Alongside this, a decrease of $\approx$40% in the omission and commission errors over OSs is observed using the θ^p_{DP} spectrum.

Similarly, over the Kuwaitian test site, we observed around 30% increase in the overall accuracy using θ^p_{DP} spectrum as compared to $(\theta^1_{\mathrm{DP}}, \theta^2_{\mathrm{DP}})$, $\approx$4% and $\approx$3% as compared to (VV, VH)

TABLE III
ACCURACY SCORES OVER DIFFERENT TARGETS USING $(\theta^1_{DP}, \theta^2_{DP})$, θ^p_{DP} SPECTRUM, AND (VV, VH) INTENSITIES FOR THE SENTINEL-1 DATA OVER THE KUWAITIAN STUDY AREA

	Overall Accuracy (%)	Omission error (%)		Commission error (%)		Kappa
		Water	OS	Water	OS	
$(\theta^1_{DP}, \theta^2_{DP})$	47.86	10.37	91.31	52.07	52.8	0.02
θ^p_{DP} **spectrum**	81.77	11.59	24.46	22.78	12.58	0.64
(VV, VH) intensities	77.82	10.42	28.79	26.13	11.97	0.61
$[H + \alpha$ **+ A] (Otsu)** [51]	79.02	10.47	26.62	20.03	16.66	0.62

TABLE IV
ACCURACY SCORES OVER DIFFERENT TARGETS USING $(\theta^1_{DP}, \theta^2_{DP})$, θ^p_{DP} SPECTRUM, AND (VV, VH) INTENSITIES FOR THE SENTINEL-1 DATA OVER THE UAE STUDY AREA

	Overall Accuracy (%)	Omission error (%)		Commission error (%)		Kappa
		Water	OS	Water	OS	
$(\theta^1_{DP}, \theta^2_{DP})$	46.78	3.78	87.71	56.65	17.68	0.07
θ^p_{DP} **spectrum**	84.72	5.29	22.25	25.19	4.54	0.7
(VV, VH) intensities	77.92	6.21	28.46	26.32	5.16	0.68
$[H + \alpha$ **+ A] (Otsu)** [51]	83.60	6.31	21.82	28.62	6.09	0.66

TABLE V
ACCURACY SCORES OVER DIFFERENT TARGETS USING $(\theta^1_{DP}, \theta^2_{DP})$, θ^p_{DP} SPECTRUM, AND (VV, VH) INTENSITIES FOR THE SENTINEL-1 DATA OVER THE MEDITERRANEAN SEA STUDY AREA

	Overall Accuracy (%)	Omission error (%)		Commission error (%)		Kappa
		Water	OS	Water	OS	
$(\theta^1_{DP}, \theta^2_{DP})$	79.81	2.46	98.27	18.61	86.24	0.01
θ^p_{DP} **spectrum**	92.09	2.47	31.88	6.91	13.78	0.71
(VV, VH) intensities	86.66	4.27	39.23	8.12	18.82	0.64
$[H + \alpha$ **+ A] (Otsu)** [51]	88.46	3.92	36.62	7.79	16.44	0.67

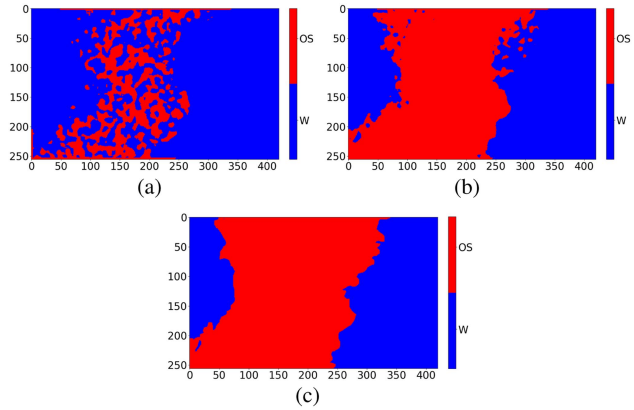

Fig. 6. Unsupervised classified maps using the K-means classifier with (a) $(\theta^1_{DP}, \theta^2_{DP})$, (b) θ^p_{DP} spectrum for Sentinel-1 SAR data over India, and (c) in situ data.

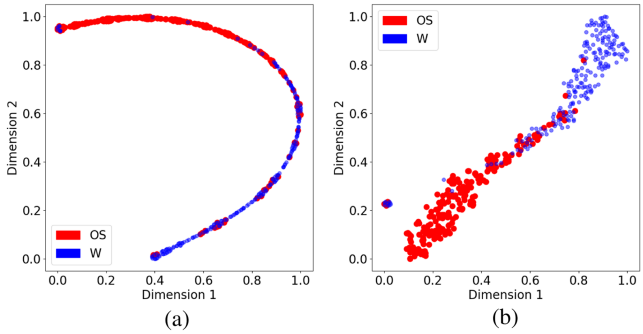

Fig. 7. t-SNE plot for (a) $(\theta^1_{DP}, \theta^2_{DP})$ and (b) θ^p_{DP} spectrum correspond to the Sentinel-1 data over Indian study area. Points in red: OS and blue: waterbody.

intensities and $[H + \alpha$ + A] based clustering, respectively, in Table III. Moreover, an overall increase of 30% over waterbody and 20% over OS is observed using θ^p_{DP} spectrum. However, the lower overall accuracy as compared to the Indian OS area might be due to the wind speed of 5.2 ms^{-1} over the ocean surface during the time of acquisition. A significant difference in the omission and commission errors is evident in this context.

Over the UAE study area, we observed an overall accuracy of 46.78% using $(\theta^1_{DP}, \theta^2_{DP})$ as observed in Table IV. On the contrary, the overall accuracy using (VV, VH) intensities is 77.92%, using $[H + \alpha$ + A] is 83.60% and using θ^p_{DP} spectrum is 84.72%. In this case, the overall accuracies between $[H + \alpha$ + A] and θ^p_{DP} spectrum are comparable. At the same time, a significant decrease in the omission error (≈60%) of the OS is also observed. Besides, the reduction in commission error is 30% over waterbody and 13% over OS. This study area also observed a significant increase in the kappa score.

Over the Mediterranean Sea study area the overall accuracy for $(\theta^1_{DP}, \theta^2_{DP})$ is 79.81% as seen in Table V. On the contrary, the accuracy using θ^p_{DP} spectrum is 92.09%. For (VV, VH) intensities and $[H + \alpha$ + A] based clustering the obtained overall accuracies are 86.66% and 88.46%, respectively. Compared to previous study areas, the omission and commission error are also lesser for both waterbody and OS using θ^p_{DP} spectrum. Moreover, improvements of kappa scores for θ^p_{DP} spectrum, (VV, VH) intensities and $[H + \alpha$ + A] based clustering are also observed.

The unsupervised clustered maps over the Indian area using Sentinel-1 data are shown in Fig. 6. One can observe that the detected OS area is much higher for θ^p_{DP} spectrum in Fig. 6(a) as compared to $(\theta^1_{DP}, \theta^2_{DP})$ in Fig. 6(b). Moreover, the predicted area of OS using θ^p_{DP} spectrum also significantly matches with the in situ measurements in Fig. 6(c). This lower predictive performance of $(\theta^1_{DP}, \theta^2_{DP})$ can also be addressed by the t-distributed Stochastic Neighborhood Embedding (t-SNE), as shown in Fig. 7. From the t-SNE plots, it can be seen that a significant proportion of points of OS and W lie over each other for $(\theta^1_{DP}, \theta^2_{DP})$ in Fig. 7(a). At the same time, distinct clusters of W and OS exist in case of θ^p_{DP} spectrum in Fig. 7(b). However, a specific portion of overlap still exists between W and OS in θ^p_{DP} spectrum, due to which the overall clustering accuracy gets impacted.

Over the Kuwaitian OS, it can be observed in Fig. 8(a) and (b) that the total number of detected pixels is much lesser than the Indian test site using $(\theta^1_{DP}, \theta^2_{DP})$. However, the detected OS pixels using θ^p_{DP} spectrum highly agree with the in situ data in Fig. 8(c). A mixture in clusters of OS and W can be observed in Fig. 9(a). Similar to the Indian test site, distinct clusters of W and OS exist in Fig. 9(b) using θ^p_{DP} spectrum.

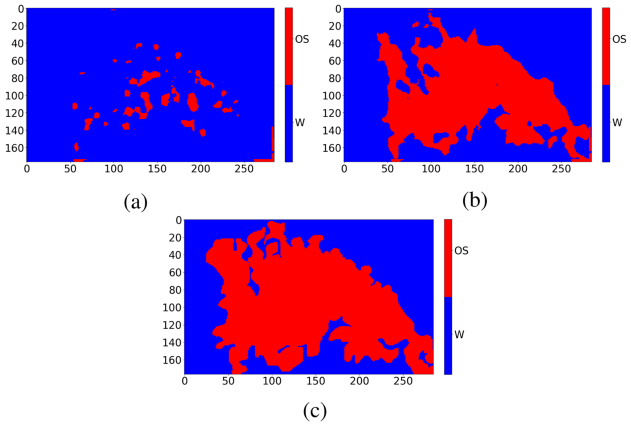

Fig. 8. Unsupervised classified maps using the K-means classifier with (a) $(\theta^1_{\mathrm{DP}}, \theta^2_{\mathrm{DP}})$, (b) θ^p_{DP} spectrum for Sentinel-1 SAR data over Kuwait, and (c) in situ data.

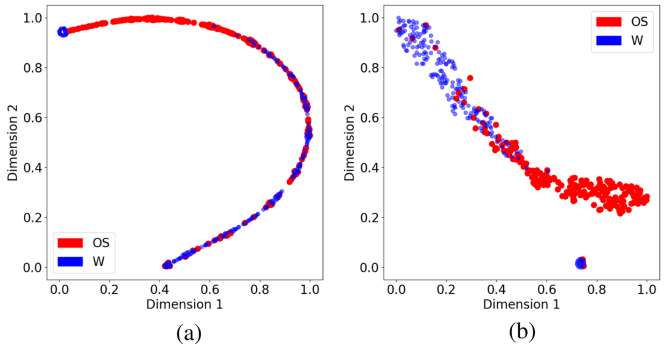

Fig. 9. t-SNE plot for (a) $(\theta^1_{\mathrm{DP}}, \theta^2_{\mathrm{DP}})$ and (b) θ^p_{DP} spectrum correspond to the Sentinel-1 data over Kuwaitian study area. Points in red: OS and blue: waterbody.

Similarly, over the UAE test site, a significant difference in the predicted pixels between $(\theta^1_{\mathrm{DP}}, \theta^2_{\mathrm{DP}})$ and θ^p_{DP} spectrum is evident in Fig. 10(a) and (b), respectively. Also, distinct clusters are observed in Fig. 11(a) compared to Fig. 11(b). For the Mediterranean Sea study area, the classified maps are shown in Fig. 12. Due to high confusion between the waterbody and the oil pixels, the classified map using $(\theta^1_{\mathrm{DP}}, \theta^2_{\mathrm{DP}})$ in Fig. 12(a) shows lesser number of OS pixels than waterbody pixels. Alternatively, the clustered map using θ^p_{DP} spectrum in Fig. 12(b) is close to the in situ measurement in Fig. 12(c). Similar difference in the confusion between $(\theta^1_{\mathrm{DP}}, \theta^2_{\mathrm{DP}})$ and θ^p_{DP} spectrum can be seen in the t-SNE plots in Fig. 13(a) and (b), respectively.

It can be seen from the clustering results that the accuracies using $(\theta^1_{\mathrm{DP}}, \theta^2_{\mathrm{DP}})$ are much lower than the θ^p_{DP} spectrum. These low accuracies can be explained with the help of the images of entropy in Fig. 14. We observed a mean entropy of 0.6 to 0.89 over W and 0.87 to 0.94 over OS area. The spatial distribution of entropy over OS and W in different test sites can be seen in Fig. 14. The reason can be interpreted with the difference between the normalized eigenvalues. We found that the difference is very low over the marine OS areas for all the test sites. This low difference is essentially due to the very low backscattering from the areas, which are less than the nominal Noise Equivalent Sigma Zero -22 dB [52].

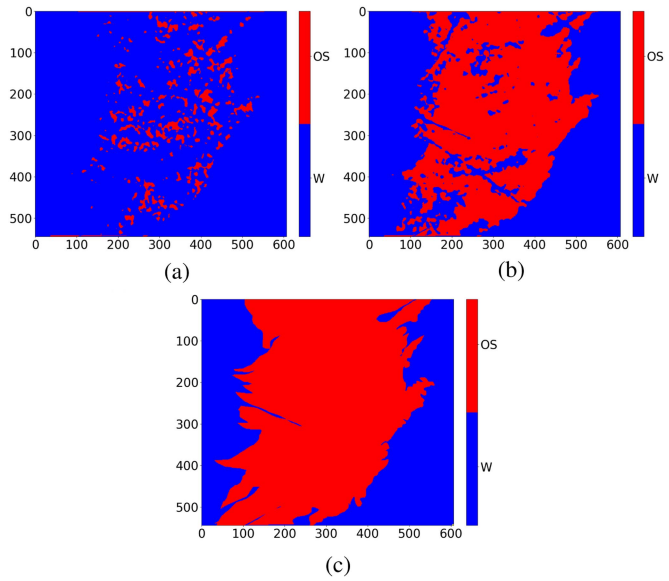

Fig. 10. Unsupervised classified maps using the K-means classifier with (a) $(\theta^1_{\mathrm{DP}}, \theta^2_{\mathrm{DP}})$, (b) θ^p_{DP} spectrum for Sentinel-1 SAR data over the UAE, and (c) in situ data.

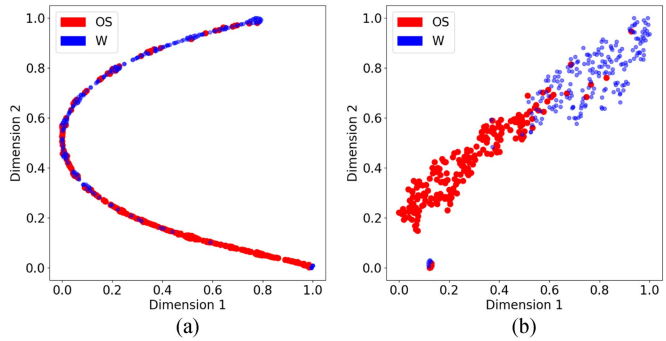

Fig. 11. t-SNE plot for (a) $(\theta^1_{\mathrm{DP}}, \theta^2_{\mathrm{DP}})$ and (b) θ^p_{DP} spectrum correspond to the Sentinel-1 data over Arabian study area. Points in red: OS and blue: waterbody.

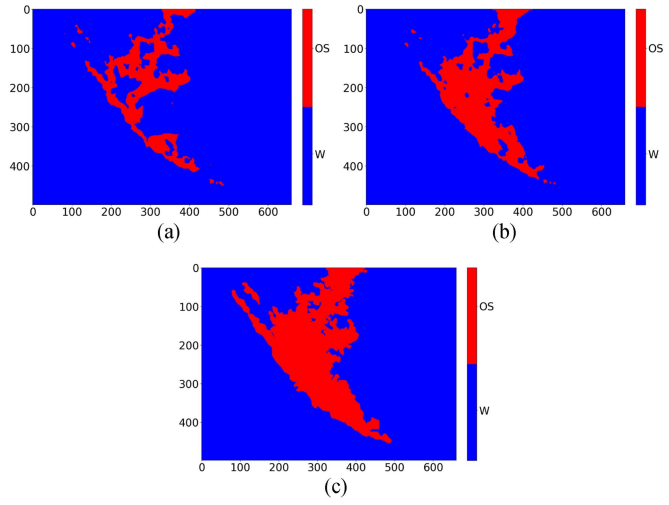

Fig. 12. Unsupervised classified maps using the K-means classifier with (a) $(\theta^1_{\mathrm{DP}}, \theta^2_{\mathrm{DP}})$, (b) θ^p_{DP} spectrum for Sentinel-1 SAR data over the Mediterranean Sea, and (c) in situ data.

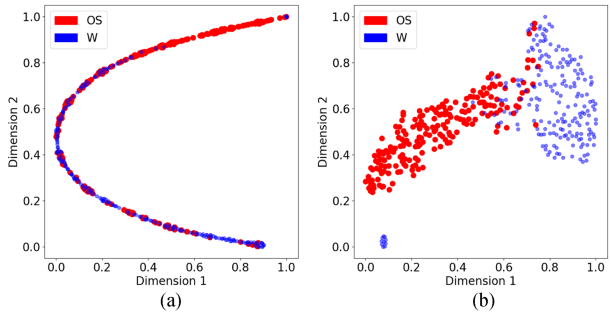

Fig. 13. t-SNE plot for (a) $(\theta^1_{\mathrm{DP}}, \theta^2_{\mathrm{DP}})$ and (b) θ^p_{DP} spectrum correspond to the Sentinel-1 data over Mediterranean Sea study area. Points in red: OS and blue: waterbody.

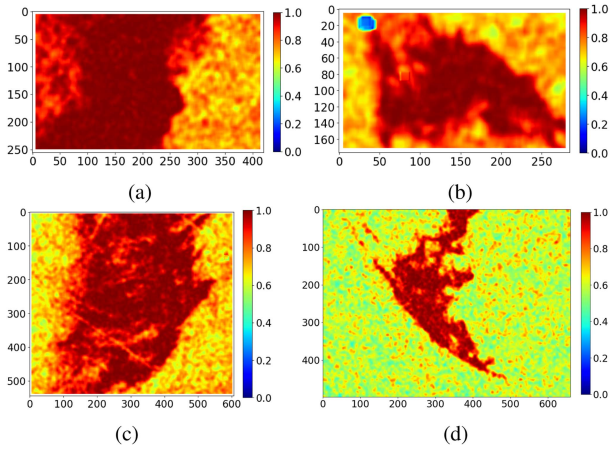

Fig. 14. Spatial images of entropy over (a) Indian test site, (b) Kuwaitian test site, (c) UAE, and (d) Mediterranean Sea test site.

On the contrary, the difference is lower in the range of 0.57 to 0.86 over the waterbody. However, a significant amount of pixels over the waterbody have a low difference between the normalized eigenvalues, while a few pixels hold these difference values ranging from 0.8 to 1. As a result, significant confusion is generated between the waterbody and OS for $(\theta^1_{\mathrm{DP}}, \theta^2_{\mathrm{DP}})$. An interesting anomaly for the entropy image is found over the Mediterranean Sea study area in Fig. 14. For this particular area, the difference in normalized eigenvalues over the waterbody, is much higher than in the other areas. This high difference might be due to the enclosed nature of the Mediterranean Sea, due to which the water circulation is primarily dominated by the salinity and temperature instead of the wind velocity [53].

V. Conclusion

This study focuses on detecting OS in the waterbody of the ocean. We offer a new DP scattering spectrum-based analysis over Sentinel 1 C-band SAR data. We have examined the random scattering vector properties. The SAR data covariance information was projected onto the scattering vectors to create a new vector with unique information. These projected scattering vectors also provide higher order covariance. Thus, Schur factorization of the additional covariance information yields second-order scattering information. Finally, this second-order information generates the target characterization parameter θ^p_{DP}DP.

First, we examined the θ^p_{DP} spectrum across W and OS pixels. The spectrum over W and OS was distinct. W, being a coherent target, centres its θ^p_{DP} spectrum at 42°. The OS area's significant SAR wave attenuation has reduced co-pol and cross-pol intensities. Thus, the OS region has strong entropy and scattering spectrum from $-45°$ to 45°.

Further, we have demonstrated the effectiveness of θ^p_{DP} spectrum using Sentinel-1 data over an Indian test site, a Kuwaitian test site, a UAE test site, and a Mediterranean test site. An unsupervised K-means clustering technique was used to classify W and OS within a resolution cell. The clustering accuracies are compared with the target characterization parameters obtained from the eigen decomposition technique, $(\theta^1_{\mathrm{DP}}, \theta^2_{\mathrm{DP}})$. θ^p_{DP} spectrum outperforms the $(\theta^1_{\mathrm{DP}}, \theta^2_{\mathrm{DP}})$ in clustering accuracy. Over the Indian, Kuwaitian, and UAE test sites, we achieved $\approx 88\%, 81\%$, and 84% overall accuracy, respectively, using θ^p_{DP} spectrum, while over the Mediterranean test site the overall accuracies is around 92.09%. These clustering accuracies are $\approx$20% to 30% higher than that obtained from $(\theta^1_{\mathrm{DP}}, \theta^2_{\mathrm{DP}})$.

Therefore, the proposed methodology agrees well with the predicted and in situ OS and W areas for C-band Sentinel-1 data. In future investigations, these results can be enhanced using various statistical methodologies. Furthermore, the findings will be helpful for future missions, including NISAR. Nonetheless, a rigorous study of wind conditions over the OS location is required to ensure clustering accuracy.

References

[1] R. Elmgren, "Understanding human impact on the baltic ecosystem: Changing views in recent decades," *AMBIO: A. J. Hum. Environ.*, vol. 30, no. 4, pp. 222–231, 2001.
[2] D. Tang, J. Sun, L. Zhou, S. Wang, R. P. Singh, and G. Pan, "Ecological response of phytoplankton to the oil spills in the oceans," *Geomatics Natural Hazards Risk*, vol. 10, no. 1, pp. 853–872, 2019.
[3] O. T. S. Statistics, *The International Tanker Owners Pollution Federation Limited*. London, U.K.: ITOPF, 2015.
[4] M. Fingas and C. E. Brown, "A review of oil spill remote sensing," *Sensors*, vol. 18, no. 1, 2017, Art. no. 91.
[5] K. P. Singh, A. L. Gray, R. K. Hawkins, and R. A. O'Neil, "The influence of surface oil on C-and Ku-band ocean backscatter," *IEEE Trans. Geosci. Remote Sens.*, vol. 5, no. 5, pp. 738–744, Sep. 1986.
[6] C. Brekke and A. H. Solberg, "Oil spill detection by satellite remote sensing," *Remote Sens. Environ.*, vol. 95, no. 1, pp. 1–13, 2005.
[7] D. Velotto, M. Migliaccio, F. Nunziata, and S. Lehner, "Dual-polarized TerraSAR-X data for oil-spill observation," *IEEE Trans. Geosci. remote Sens.*, vol. 49, no. 12, pp. 4751–4762, Dec. 2011.
[8] A. Buono, F. Nunziata, C. R. de Macedo, D. Velotto, and M. Migliaccio, "A sensitivity analysis of the standard deviation of the copolarized phase difference for sea oil slick observation," *IEEE Trans. Geosci. Remote Sens.*, vol. 57, no. 4, pp. 2022–2030, Apr. 2019.
[9] F. Nunziata, A. Gambardella, and M. Migliaccio, "On the mueller scattering matrix for SAR sea oil slick observation," *IEEE Geosci. Remote Sens. Lett.*, vol. 5, no. 4, pp. 691–695, Oct. 2008.
[10] M. Migliaccio, F. Nunziata, and A. Gambardella, "On the co-polarized phase difference for oil spill observation," *Int. J. Remote Sens.*, vol. 30, no. 6, pp. 1587–1602, 2009.
[11] A.-B. Salberg, Ø. Rudjord, and A. H. S. Solberg, "Oil spill detection in hybrid-polarimetric SAR images," *IEEE Trans. Geosci. Remote Sens.*, vol. 52, no. 10, pp. 6521–6533, Oct. 2014.
[12] Y. Guo and H. Z. Zhang, "Oil spill detection using synthetic aperture radar images and feature selection in shape space," *Int. J. Appl. Earth Observ. Geoinformation*, vol. 30, pp. 146–157, 2014.
[13] S. Skrunes, C. Brekke, and T. Eltoft, "Characterization of marine surface slicks by Radarsat-2 multipolarization features," *IEEE Trans. Geosci. Remote Sens.*, vol. 52, no. 9, pp. 5302–5319, Nov. 2013.

[14] D. Mera, J. M. Cotos, J. Varela-Pet, P. G. Rodríguez, and A. Caro, "Automatic decision support system based on SAR data for oil spill detection," *Comput. Geosciences*, vol. 72, pp. 184–191, 2014.
[15] S. Singha, D. Velotto, and S. Lehner, "Near real time monitoring of platform sourced pollution using TerraSAR-X over the North Sea," *Mar. Pollut. Bull.*, vol. 86, no. 1/2, pp. 379–390, 2014.
[16] M. Marghany, "Utilization of a genetic algorithm for the automatic detection of oil spill from RADARSAT-2 SAR satellite data," *Mar. Pollut. Bull.*, vol. 89, no. 1/2, pp. 20–29, 2014.
[17] F. Nunziata, A. Buono, and M. Migliaccio, "Cosmo–skymed synthetic aperture radar data to observe the deepwater horizon oil spill," *Sustainability*, vol. 10, no. 10, 2018, Art. no. 3599.
[18] Y. Chen and Z. Wang, "Marine oil spill detection from SAR images based on attention U-Net model using polarimetric and wind speed information," *Int. J. Environ. Res. Public Health*, vol. 19, no. 19, 2022, Art. no. 12315.
[19] S. K. Chaturvedi, S. Banerjee, and S. Lele, "An assessment of oil spill detection using Sentinel 1 SAR-C images," *J. Ocean Eng. Sci.*, vol. 5, no. 2, pp. 116–135, 2020.
[20] C. Alexandrov, N. Kolev, Y. Sivkov, A. Hristov, and M. Tsvetkov, "Oil spills detection on sea surface by using Sentinel-1 SAR images," in *Proc. 21st Int. Symp. Elect. App. Technol.*, 2020, pp. 1–4.
[21] L. Cheng, Y. Li, X. Zhang, and M. Xie, "An analysis of the optimal features for Sentinel-1 oil spill datasets based on an improved J–M/K-Means algorithm," *Remote Sens.*, vol. 14, no. 17, 2022, Art. no. 4290.
[22] S. Cloude, "The dual polarization entropy/alpha decomposition: A PALSAR case study," *Sci. Appl. SAR Polarimetry Polarimetric Interferometry*, vol. 644, 2007, Art. no. 2.
[23] I. A. El-Magd, M. Zakzouk, A. M. Abdulaziz, and E. M. Ali, "The potentiality of operational mapping of oil pollution in the Mediterranean Sea near the entrance of the Suez Canal using Sentinel-1 SAR data," *Remote Sens.*, vol. 12, no. 8, 2020, Art. no. 1352.
[24] L. W. Mdakane and W. Kleynhans, "Feature selection and classification of oil spill from vessels using Sentinel-1 wide–swath synthetic aperture radar data," *IEEE Geosci. Remote Sens. Lett.*, vol. 19, no. 19, Oct. 2020, Art. no. 4002505.
[25] S. Rajendran et al., "Detection of Wakashio oil spill off Mauritius using Sentinel-1 and 2 data: Capability of sensors, image transformation methods and mapping," *Environ. Pollut.*, vol. 274, 2021, Art. no. 116618.
[26] E. Bayramov, M. Kada, and M. Buchroithner, "Monitoring oil spill hotspots, contamination probability modelling and assessment of coastal impacts in the Caspian Sea using SENTINEL-1, LANDSAT-8, RADARSAT, ENVISAT and ERS satellite sensors," *J. Oper. Oceanogr.*, vol. 11, no. 1, pp. 27–43, 2018.
[27] Y. Li, X. Lyu, A. C. Frery, and P. Ren, "Oil spill detection with multiscale conditional adversarial networks with small-data training," *Remote Sens.*, vol. 13, no. 12, 2021, Art. no. 2378.
[28] Y. Li, W. Huang, X. Lyu, S. Liu, Z. Zhao, and P. Ren, "An adversarial learning approach to forecasted wind field correction with an application to oil spill drift prediction," *Int. J. Appl. Earth Observ. Geoinformation*, vol. 112, 2022, Art. no. 102924.
[29] X. Ma, J. Xu, P. Wu, and P. Kong, "Oil spill detection based on deep convolutional neural networks using polarimetric scattering information from Sentinel-1 SAR images," *IEEE Trans. Geosci. Remote Sens.*, vol. 60, 2021, Art. no. 4204713.
[30] J. Zhang et al., "Oil spill detection with dual-polarimetric Sentinel-1 SAR using superpixel-level image stretching and deep convolutional neural network," *Remote Sens.*, vol. 14, no. 16, 2022, Art. no. 3900.
[31] S. Ahmed, T. ElGharbawi, M. Salah, and M. El-Mewafi, "Deep neural network for oil spill detection using Sentinel-1 data: Application to Egyptian coastal regions," *Geomatics, Natural Hazards Risk*, vol. 14, no. 1, pp. 76–94, 2023.
[32] J. Fan and C. Liu, "Multitask GANs for oil spill classification and semantic segmentation based on SAR images," *IEEE J. Sel. Topics Appl. Earth Observ. Remote Sens.*, vol. 16, no. 16, pp. 2532–2546, Feb. 2023.
[33] S. Dey, N. Romero-Puig, and A. Bhattacharya, "Polarimetric scattering spectrum analysis for target characterization," *IEEE Geosci. Remote Sens. Lett.*, vol. 19, no. 19, Sep. 2022, Art. no. 4027005.
[34] X. Ma, J. Xu, P. Wu, and P. Kong, "Oil spill detection based on deep convolutional neural networks using polarimetric scattering information from Sentinel-1 SAR images," *IEEE Trans. Geosci. Remote Sens.*, vol. 60, no. 60, Nov. 2022, Art. no. 4204713.
[35] S. Dey, N. Bhogapurapu, S. Homayouni, A. Bhattacharya, and H. McNairn, "Unsupervised classification of crop growth stages with scattering parameters from dual-pol Sentinel-1 SAR data," *Remote Sens.*, vol. 13, no. 21, 2021, Art. no. 4412.
[36] R. Barakat, "Degree of polarization and the principal idempotents of the coherency matrix," *Opt. Commun.*, vol. 23, no. 2, pp. 147–150, 1977.
[37] C. Yuan and H. Yang, "Research on K-value selection method of K-means clustering algorithm," *J*, vol. 2, no. 2, pp. 226–235, 2019.
[38] T. Kanungo, D. M. Mount, N. S. Netanyahu, C. D. Piatko, R. Silverman, and A. Y. Wu, "An efficient K-means clustering algorithm: Analysis and implementation," *IEEE Trans. Pattern Anal. Mach. Intell.*, vol. 24, no. 7, pp. 881–892, Jul. 2002.
[39] L. V. D. Maaten and G. Hinton, "Visualizing data using t-SNE," *J. Mach. Learn. Res.*, vol. 9, no. Nov., pp. 2579–2605, 2008.
[40] S. Prasad, T. Balakrishnan Nair, H. Rahaman, S. Shenoi, and T. Vijayalakshmi, "An assessment on oil spill trajectory prediction: Case study on oil spill off Ennore port," *J. Earth System Sci.*, vol. 127, pp. 1–8, 2018.
[41] K. Dasari, L. Anjaneyulu, and J. Nadimikeri, "Application of C-band Sentinel-1 A SAR data as proxies for detecting oil spills of Chennai, East Coast of India," *Mar. Pollut. Bull.*, vol. 174, 2022, Art. no. 113182.
[42] M. M. Nezhad, D. Groppi, G. Laneve, P. Marzialetti, and G. Piras, "Oil spill detection analyzing "Sentinel 2" satellite images: A Persian Gulf case study," in *Proc. 3rd World Congr. Civil, Structural, Environ. Eng.*, 2018, pp. 1–8.
[43] S. Naz, M. F. Iqbal, I. Mahmood, and M. Allam, "Marine oil spill detection using synthetic aperture radar over Indian Ocean," *Mar. Pollut. Bull.*, vol. 162, 2021, Art. no. 111921.
[44] F. A. Gafoor and M. R. Al Shehhi, "Oil spill detection and mapping using Sentinel-1 and Sentinel-2 in the Arabian Gulf coastal waters," in *Proc. IEEE Int. Geosci. Remote Sens. Symp.*, 2022, pp. 6745–6748.
[45] N. Issa and S. Vempatti, "Oil spills in the Arabian Gulf: A case study and environmental review," *Environ. Natural Resour. Res.*, vol. 8, no. 1, pp. 144–153, 2018.
[46] R. Al-Ruzouq et al., "Sensors, features, and machine learning for oil spill detection and monitoring: A review," *Remote Sens.*, vol. 12, no. 20, 2020, Art. no. 3338.
[47] M. S. Zaki, M. M. Authman, N. S. Ata, M. Abdelzaher, and A. Hammam, "Effects of environmental oil spills on commercial fish and shellfish in Suez Canal and Suez Gulf regions," *Life Sci. J.*, vol. 11, no. 2, pp. 269–274, 2014.
[48] M. E. Fletcher, "The Suez Canal and world shipping, 1869-1914," *J. Econ. Hist.*, vol. 18, no. 4, pp. 556–573, 1958.
[49] M. Migliaccio, F. Nunziata, A. Montuori, X. Li, and W. G. Pichel, "A multifrequency polarimetric SAR processing chain to observe oil fields in the Gulf of Mexico," *IEEE Trans. Geosci. Remote Sens.*, vol. 49, no. 12, pp. 4729–4737, Dec. 2011.
[50] K. Topouzelis and A. Psyllos, "Oil spill feature selection and classification using decision tree forest on SAR image data," *ISPRS J. Photogrammetry Remote Sens.*, vol. 68, pp. 135–143, 2012.
[51] P. Liu, X. Li, J. J. Qu, W. Wang, C. Zhao, and W. Pichel, "Oil spill detection with fully polarimetric UAVSAR data," *Mar. Pollut. Bull.*, vol. 62, no. 12, pp. 2611–2618, 2011.
[52] V. Corcione, A. Buono, F. Nunziata, and M. Migliaccio, "A sensitivity analysis on the spectral signatures of low-backscattering sea areas in Sentinel-1 SAR images," *Remote Sens.*, vol. 13, no. 6, 2021, Art. no. 1183.
[53] T. Tanhua, D. Hainbucher, K. Schroeder, V. Cardin, M. Álvarez, and G. Civitarese, "The Mediterranean Sea system: A review and an introduction to the special issue," *Ocean Sci.*, vol. 9, no. 5, pp. 789–803, 2013.

Avrodeep Paul (Member, IEEE) received the B.Tech. degree in agricultural engineering from the Sam Higginbottom University of Agriculture Technology and Sciences, Prayagraj, India, in 2021, the M.Tech. degree in aquacultural engineering from the Department of Agricultural and Food Engineering, Indian Institute of Technology Kharagpur, Kharagpur, India, in 2023. He is currently working toward the Ph.D. degree in advanced earth observation systems to assess the effects of land use and climate change on soil erosion risk with Remote Sensing and Agro-informatics Lab, Jacob Blaustein Institutes for Desert Research, Ben-Gurion University (BGU) of Negev, Beersheba, Israel.

His research interests include aquacultural rafts and oil spill detection using synthetic aperture radar, hyperspectral remote sensing, and applications of advanced earth observation systems on soil erosion risk and climate change.

Mr. Paul was a recipient of the AICTE GATE scholarship from 2021 to 2023, and is currently the recipient of the STEM Scholarship from 2023 to 2027. He is also a member of the IEEE India Council Student Coordination Team 2023.

Subhadip Dey (Member, IEEE) received the B.Tech. degree in agricultural engineering from Bidhan Chandra Krishi Viswavidyalaya, Haringhata, India, in 2016, the M.Tech. degree in aquacultural engineering from the Department of Agricultural and Food Engineering, Indian Institute of Technology Kharagpur, Kharagpur, India, in 2018, and the Ph.D. degree in microwave remote sensing in agriculture from the Indian Institute of Technology Bombay, Mumbai, India, in 2021.

He is currently an Assistant Professor with the Agricultural and Food Engineering Department, Indian Institute of Technology Kharagpur. Before this position, he was associated with the Deutsches Zentrum for Luft- und Raumfahrt (German Aerospace Center), Cologne, Germany, as a Postdoctoral Researcher. His current research interests are applications of microwave remote sensing in aquaculture and agriculture.

Dr. Dey was a recipient of prestigious Humboldt fellowship and DLR-DAAD postdoctoral fellowship.

Armando Marino (Member, IEEE) received the M.Sc. degree in telecommunication engineering from the Universita' di Napoli "Federico II," Naples, Naples, Italy, in 2006 and the Ph.D. degree in polarimetric SAR interferometry from the School of Geosciences, University of Edinburgh, Edinburgh, U.K., in 2011.

In 2006, he joined the High Frequency and Radar Systems Department, German Aerospace Centre, Oberpfaffenhofen, Germany, where he developed his M.Sc. thesis. In 2011, he was with the University of Alicante, Institute of Computing Research, Madrid, Spain. From 2011 to 2015, he was a Postdoctoral Researcher and Lecturer with the Institute of Environmental Engineering, ETH Zurich, Zurich, Switzerland. In 2015, he was a Lecturer with the School of Engineering and Innovation, Open University, Milton Keynes, U.K. Since 2018, he has been an Associate Professor with the University of Stirling, Faculty of Natural Sciences, Stirling, U.K.

Gourav Dhar Bhowmick received the joint M.Tech. - Ph.D. degree in aquacultural engineering from the Agricultural and Food Engineering Department, Indian Institute of Technology Kharagpur, Kharagpur, India, in 2020.

He is currently an Assistant Professor with the Indian Institute of Technology Kharagpur. Before this position, he was associated with the Ben-Gurion University of the Negev, Beersheba, Israel, as a Postdoctoral Researcher. His current research interests are 3-D agricultural systems for urban farming, end-of-pipe treatment of marine and freshwater recirculating aquaculture systems with a focus on nitrification, phosphorous removal, and biogas production in line with residual resources engineering for environmental remediation, and seaweed-based by-product recovery.

Dr. Bhowmick was a recipient of the prestigious GYTI Award—2016 in India and the BCSC Postdoctoral Fellowship in Israel.

Avik Bhattacharya (Senior Member, IEEE) received the integrated M.Sc. degree in mathematics from the Indian Institute of Technology Kharagpur, Kharagpur, India, in 2000 and the Ph.D. degree in remote sensing image processing and analysis from Télécom ParisTech, Paris, France, and the Ariana Research Group, Institut National de Recherche en Informatique et en Automatique (INRIA), Sophia Antipolis, Nice, France, in 2007.

He is currently a Professor with the Centre of Studies in Resources Engineering, Indian Institute of Technology Bombay (CSRE, IITB), Mumbai, India. Before joining IITB, he was a Canadian Government Research Fellow with the Canadian Centre for Remote Sensing (CCRS), Ottawa, ON, Canada. His current research interests include SAR polarimetry, statistical analysis of polarimetric SAR images, applications of Radar Remote Sensing in Agriculture, Cryosphere, Urban, and Planetary studies.

Dr. Bhattacharya was the recipient of the Natural Sciences and Engineering Research Council of Canada visiting scientist fellowship at the Canadian National Laboratories, from 2008 to 2011. He is the Editor-in-Chief of IEEE GEOSCIENCE AND REMOTE SENSING LETTERS (GRSL). He was an Associate Editor of IEEE GRSL. He has been the Guest Editor of the special issue on Applied Earth Observations and Remote Sensing in India in IEEE JOURNAL OF SELECTED TOPICS IN APPLIED EARTH OBSERVATIONS AND REMOTE SENSING (J-STARS), 2017. He was one of the guest editors of the special stream on Advanced Statistical Techniques in SAR Image Processing and Analysis in IEEE GEOSCIENCE AND REMOTE SENSING LETTERS, 2018. He is the Founding Chairperson of the IEEE Geoscience and Remote Sensing Society (GRSS) Chapter of the Bombay Section. He is currently leading the Microwave Remote Sensing Lab at CSRE, IITB.